A&A 630, L2 (2019)
https://doi.org/10.1051/0004-6361/201936372

Astronomy & Astrophysics

LETTER TO THE EDITOR

Discovery of two new magnesium-bearing species in IRC+10216: MgC_3N and MgC_4H⋆

J. Cernicharo[1], C. Cabezas[1], J. R. Pardo[1], M. Agúndez[1], C. Bermúdez[1], L. Velilla-Prieto[1,2], F. Tercero[3], J. A. López-Pérez[3], J. D. Gallego[3], J. P. Fonfría[1], G. Quintana-Lacaci[1], M. Guélin[4], and Y. Endo[5]

[1] Grupo de Astrofísica Molecular. Instituto de Física Fundamental (IFF-CSIC), C/Serrano 121, 28006 Madrid, Spain
e-mail: jose.cernicharo@csic.es
[2] Department of Space, Earth and Environment, Chalmers University of Technology, Onsala Space Observatory, 439 92 Onsala, Sweden
[3] Centro de Desarrollos Tecnológicos, Observatorio de Yebes (IGN), 19141 Yebes, Guadalajara, Spain
[4] Institut de Radioastronomie Millimétrique, 300 rue de la Piscine, 38406 Saint Martin d'Hères, France
[5] Department of Applied Chemistry, Science Building II, National Chiao Tung University, 1001 Ta-Hsueh Rd., Hsinchu 30010, Taiwan

Received 24 July 2019 / Accepted 20 August 2019

ABSTRACT

We report on the detection of two series of harmonically related doublets in IRC +10216. From the observed frequencies, the rotational constant of the first series is B = 1380.888 MHz and that of the second series is B = 1381.512 MHz. The two series correspond to two species with a $^2\Sigma$ electronic ground state. After considering all possible candidates, and based on quantum chemical calculations, the first series is assigned to MgC_3N and the second to MgC_4H. For the latter species, optical spectroscopy measurements support its identification. Unlike diatomic metal-containing molecules, the line profiles of the two new molecules indicate that they are formed in the outer layers of the envelope, as occurs for MgNC and other polyatomic metal-cyanides. We also confirm the detection of MgCCH that was previously reported from the observation of two doublets. The relative abundance of MgC_3N with respect to MgNC is close to one while that of MgC_4H relative to MgCCH is about ten. The synthesis of these magnesium cyanides and acetylides in IRC +10216 can be explained in terms of a two-step process initiated by the radiative association of Mg^+ with large cyanopolyynes and polyynes followed by the dissociative recombination of the ionic complexes.

Key words. molecular data – line: identification – stars: carbon – circumstellar matter – stars: individual: IRC+10216 – astrochemistry

1. Introduction

Metal-containing molecules are rarely observed in the interstellar medium, but are widely detected in circumstellar envelopes around evolved stars. Stable closed-shell diatomic molecules containing Al, Na, or K and a halogen atom have been detected in the prototypical carbon star envelope IRC +10216 (Cernicharo & Guélin 1987). These species are mostly formed in the hot inner parts of the envelope, close to the star. Metals like Na, K, Ca, Cr, and Fe are found to survive in the gas phase as neutral and/or ionized atoms in the outer layers of IRC +10216 (Mauron & Huggins 2010), which points to a very rich metal chemistry in the cool outer envelope. Various triatomic metal cyanides (M−NC or/and M−CN) containing Mg, Na, Al, Si, K, Fe, and Ca (most of which are open-shell radicals) have been detected in IRC +10216 (Kawaguchi et al. 1993; Turner et al. 1994; Ziurys et al. 1995, 2002; Guélin et al. 2000, 2004; Pulliam et al. 2010; Zack et al. 2011; Cernicharo et al. 2019). Guélin et al. (1993) studied the spatial distribution of MgNC and concluded that this radical arises from a shell located at 15″ from the star.

The only tetratomic metal-bearing species detected so far in IRC +10216 is HMgNC (Cabezas et al. 2013). A pentatomic species, MgC_3N, was postulated by Petrie et al. (2003) as a potential abundant species in IRC +10216. They suggested that a series of doublets with rotational constant around 1395 MHz, although initially assigned to an electronic excited state of C_6H by Aoki (2000), were in fact produced by MgC_3N. However, Cernicharo et al. (2008) have shown that these doublets certainly belong to the $^2\Sigma$ state of the ν_{11} bending mode of C_6H in its $^2\Pi$ ground electronic state. Nevertheless, MgC_3N, together with MgC_4H, which could be formed in the cold outer layers of IRC +10216, are interesting molecules to be searched for in this object.

Sensitive line surveys can be used as the magic tool to reveal the molecular content of astronomical sources and to search for new molecules. Once we are able to identify the lines coming from the isotopologues and vibrationally excited states of known molecules, then a forest of unidentified lines appear that provide the opportunity to discover new molecules and insights into the chemistry and chemical evolution of the observed object.

⋆ Based on observations carried out with the IRAM 30 m telescope and the Yebes 40 m telescope. IRAM is supported by INSU/CNRS (France), MPG (Germany) and IGN (Spain). The 40 m radiotelescope at Yebes Observatory is operated by the Spanish Geographic Institute (IGN, Ministerio de Fomento).

In this Letter we report the discovery of two new series of doublets with very close rotational constants (1380.9 MHz and 1381.5 MHz) produced by two new molecular species having a $^2\Sigma$ ground electronic state. On the basis of precise quantum chemical calculations and an exploration of all possible candidates, we assign these lines to MgC_3N and MgC_4H.

2. Observations

The observations at 3 mm presented in this paper were carried out with the IRAM 30 m radio telescope and have been described in detail by Cernicharo et al. (2019). Briefly, the data in the 3 mm window correspond to observations acquired during the last 35 years and cover the 70–116 GHz domain with very high sensitivity (1–3 mK). Examples of these data can be found in Cernicharo et al. (2004, 2007, 2008, 2019) and Agúndez et al. (2008, 2014). The observing mode, where we wobbled the secondary mirror by ±90″ at a rate of 0.5 Hz, ensured flat baselines. This observing method provides reference data free from emission from all molecules but CO (see Cernicharo et al. 2015). The emission of all other molecular species is restricted to a region ≤15–20″ from the star (see e.g. Guélin et al. 1993; Agúndez et al. 2015, 2017; Velilla et al. 2015; Quintana-Lacaci et al. 2016).

The observations in the Q band (32–50 GHz) were performed in May and June 2019 with the 40 m radiotelescope of the Centro Astronómico de Yebes (IGN, Spain). New receivers built for the European Research Council synergy project Nanocosmos were installed at the telescope and used for these observations during its commissioning phase. The experimental set-up will be described in detail by Tercero et al. (in prep.). Briefly, the Q-band receiver consists of two HEMT cold amplifiers covering the 32–50 GHz band with horizontal and perpendicular polarizations. Receiver temperatures vary from 22 K at 32 GHz up to 42 K at 50 GHz. The spectrometers are 16 × 2.5 GHz FFTs with a spectral resolution of 38.1 kHz providing the whole coverage of the Q-band in both polarizations. The total observing time on-source for the observations presented here corresponds to ~24 h. The observing mode was position switching with an off position at 300″ in azimuth.

Pointing corrections were obtained by observing strong nearby quasars and the SiO masers of R Leo. Pointing errors were always within 2–3″. The intensity scale, antenna temperature (T_A^*), was corrected for atmospheric absorption using the ATM package (Cernicharo 1985; Pardo et al. 2001). The beam size of the IRAM 30 m telescope in the 3 mm domain is 21–30″, while for the 40 m telescope the beam size in the Q band is in the range 36–56″. The main beam efficiency of the 40 m telescope varies between 60% at 32 GHz and 50% at 50 GHz. Calibration uncertainties of 10% were adopted for data covering such a long observing period in the 3 mm domain. A similar uncertainty was assumed for the data in the Q band. Additional uncertainties could arise from the line intensity fluctuation with time induced by the variation of the stellar infrared flux (Cernicharo et al. 2014; Pardo et al. 2018). All data were analysed using the GILDAS package[1].

3. Results

In the IRAM 30 m data we found a series of doublets (S 1) whose components are separated by ~4.3 MHz. The doublets are in harmonic relation with integer quantum numbers from N_{up} = 26 to N_{up} = 40. Some of these doublets show some overlap with other features, as shown in Figs. 1 and 2. As a first step we verified that no other harmonic relation can apply and the lines cannot be due to any known species. Once we were sure that the doublets belong to a new molecular species, we searched for the corresponding doublets in the Q band, which correspond to quantum numbers from N_{up} = 12 to N_{up} = 18. All them were detected and are shown in Fig. 1. Interestingly, none of these doublets are present in the previous survey of IRC +10216 in the Q band performed with the Nobeyama radiotelescope (Kawaguchi et al. 1995). This is due to the higher sensitivity of our data, less than 1 mK (see Fig. 1) versus 5 mK in the Nobeyama data. Finally, a total of 22 doublets (see Figs. 1 and 2) were found between the Q and the 3 mm bands. Their frequencies are given in Table A.1. From a fit to the observed frequencies, we obtain the following rotational, distortion, and spin-rotation constants:

B = 1380.888 ± 0.001 MHz

D = 0.0760 ± 0.0005 kHz

γ = 4.35 ± 0.04 MHz.

After a careful examination of the data we realized that some unidentified features located on the right side of the S 1 doublets are in fact harmonically related doublets with integer quantum numbers (S 2). They are indicated by magenta arrows in Figs. 1 and 2. The S 2 doublets have the same quantum numbers as S 1 and correspond to a $^2\Sigma$ molecule. The frequencies of S 2, given in Table A.2, are fitted with the following constants:

B = 1381.512 ± 0.004 MHz

D = 0.074 ± 0.002 kHz

γ = 4.7 ± 0.1 MHz.

A detailed analysis of possible carriers for S 1 and S 2 is given in Appendix B. After discarding all plausible molecular species, we conclude that our best candidates are metal-bearing species attached to a C_3N or C_4H group. Species containing Na or Al attached to C_3N or C_4H groups have singlet ground electronic states and therefore cannot be the carriers of S 1 and S 2. In fact, AlC_3N and NaC_3N have been observed in the laboratory (Cabezas et al. 2014, 2019) and their rotational constants are too low with respect to those quoted above for S 1 and S 2. In contrast, molecular species containing Mg or Ca present $^2\Sigma$ electronic states and they are postulated as the candidates responsible for the S 1 and S 2 rotational transitions. In a previous paper, Cabezas et al. (2019) reported ab initio calculations for both MgC_3N and CaC_3N species. The calculated rotational constant for MgC_3N indicates that this molecule could be one of the carriers of S 1 or S 2. On the other hand, the rotational constant of CaC_3N is much smaller than those of S 1 and S 2, discarding Ca as a candidate. Hence, we performed high-level quantum chemical calculations for both MgC_4H and MgC_3N (see Appendix C). For MgC_3N we obtain B = 1376.5 MHz, D = 0.065 kHz, and γ = 4.1 MHz. For MgC_4H we obtained a slightly higher value of B, 1377.4 MHz, D = 0.061 kHz, and γ = 4.4 MHz. All these results are given in Appendix C.

High-resolution optical spectroscopy of the $A^2\Pi - X^2\Sigma$ electronic transition of MgC_4H were performed by Ding et al. (2008) and Chasovskikh et al. (2008). They obtain a rotational constant of B = 1384.7 ± 6 MHz. Subsequent observations of the same electronic transition of MgC_4H by Forthomme et al. (2010) provide a much more accurate value for the rotational constant, B = 1380.9 ± 0.2 MHz. The spectral resolution of these observations is 0.002 cm^{-1} (~60 MHz) and near 250 transitions have been observed with upper quantum numbers up to

[1] http://www.iram.fr/IRAMFR/GILDAS

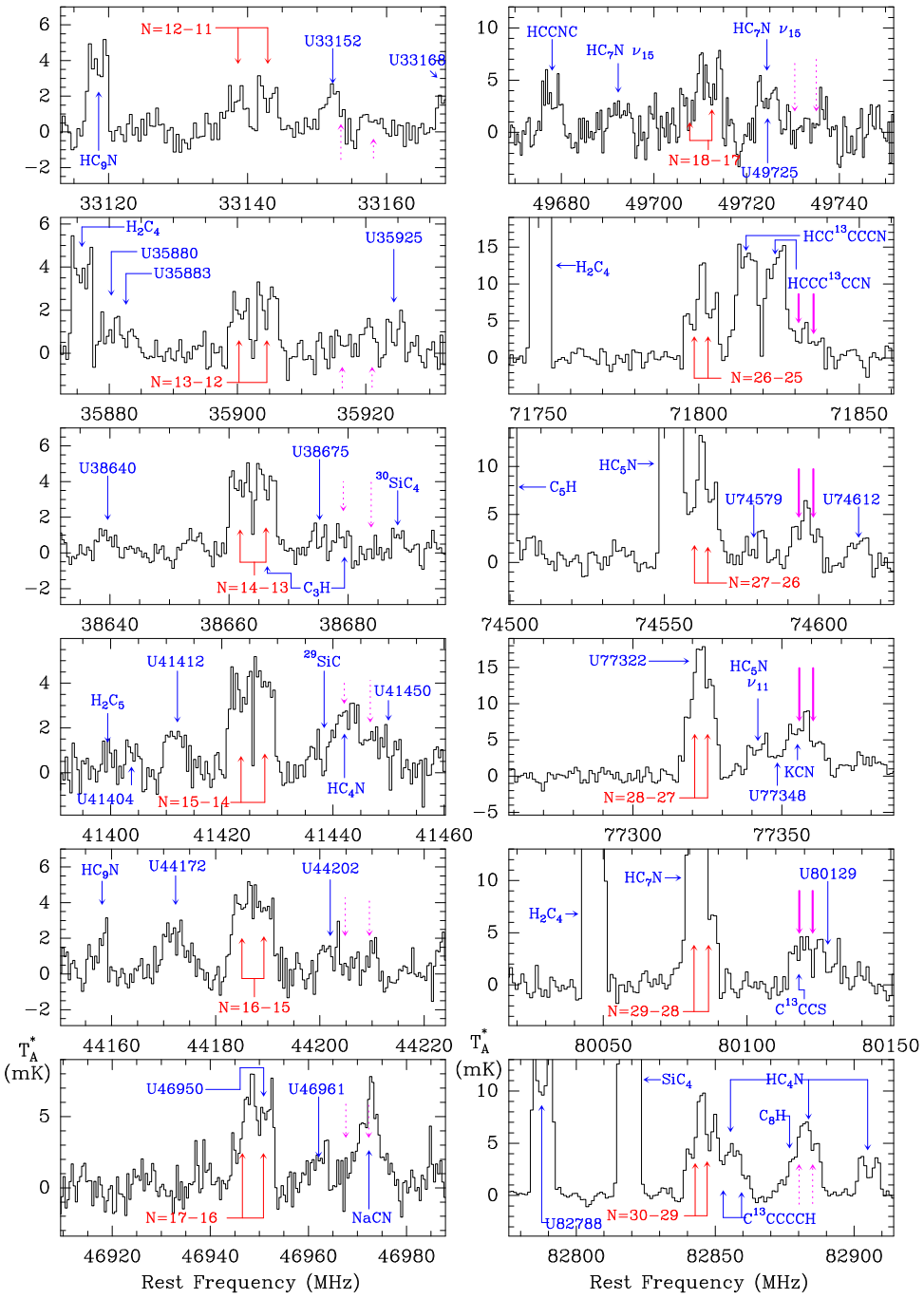

Fig. 1. Observed doublets towards IRC+10216 (black histogram). The vertical scale is the antenna temperature in mK and the horizontal scale is the rest frequency in MHz. Shown are the lines of the series of doublets $S\,1$ (labelled in red) and those of series $S\,2$, with the same quantum numbers as $S\,1$ (in magenta); unidentified (U) lines and lines arising from other species are also shown (in blue). When lines of the $S\,2$ series are blended with other features, or are too weak to be detected (those below 50 GHz), their positions are indicated by dashed arrows.

$N = 42$. Hence, the derived rotational constant and its uncertainty are highly confident. Using the relation $D = B^3/\omega^2$, these authors estimated the distortion constant to be 0.077 kHz. Hence, either of the two series $S\,1$ or $S\,2$ may be assigned to MgC_4H. The calculated dipole moment of MgC_3N is 6.3 D and that of MgC_4H 2.1 D (see Appendix C). Consequently, both species will harbour a different line intensity distribution with quantum number N. We consider that MgC_4H is responsible for the $S\,2$ series as its dipole moment of 2.1 D produces rotational transitions in IRC +10216 peaking in the 3 mm domain with weak emission below 50 GHz. Consequently, the $S\,1$ series is assigned to MgC_3N because with its high dipole moment its rotational transitions are strong in the Q band and will start to decline in intensity for high values of N in the 3 mm band (similar to the behaviour of HC_5N). Moreover, all quantum chemical calculations indicate that the rotational constant of MgC_4H is slightly larger than that of MgC_3N, as observed for $S\,2$ and $S\,1$. Consequently, we conclude that we have detected, and fully characterized spectroscopically in space, the magnesium-bearing species MgC_3N ($S\,1$) and MgC_4H ($S\,2$). The definitive confirmation will require laboratory rotational spectroscopy. We also present new observations (see Appendix E) that confirm the tentative detection of MgCCH in IRC +10216 reported by Agúndez et al. (2014).

4. Discussion

The observed line intensities of MgC_3N can be fit to two components, a cold one with a rotational temperature of 15 ± 2 K and a column density of $(5.7 \pm 1.0) \times 10^{12}$ cm^{-2}, and a warm one with $T_{\rm rot} = 34 \pm 6$ K and $N = (3.6 \pm 0.6) \times 10^{12}$ cm^{-2}. For MgC_4H we derive a relatively high rotational temperature

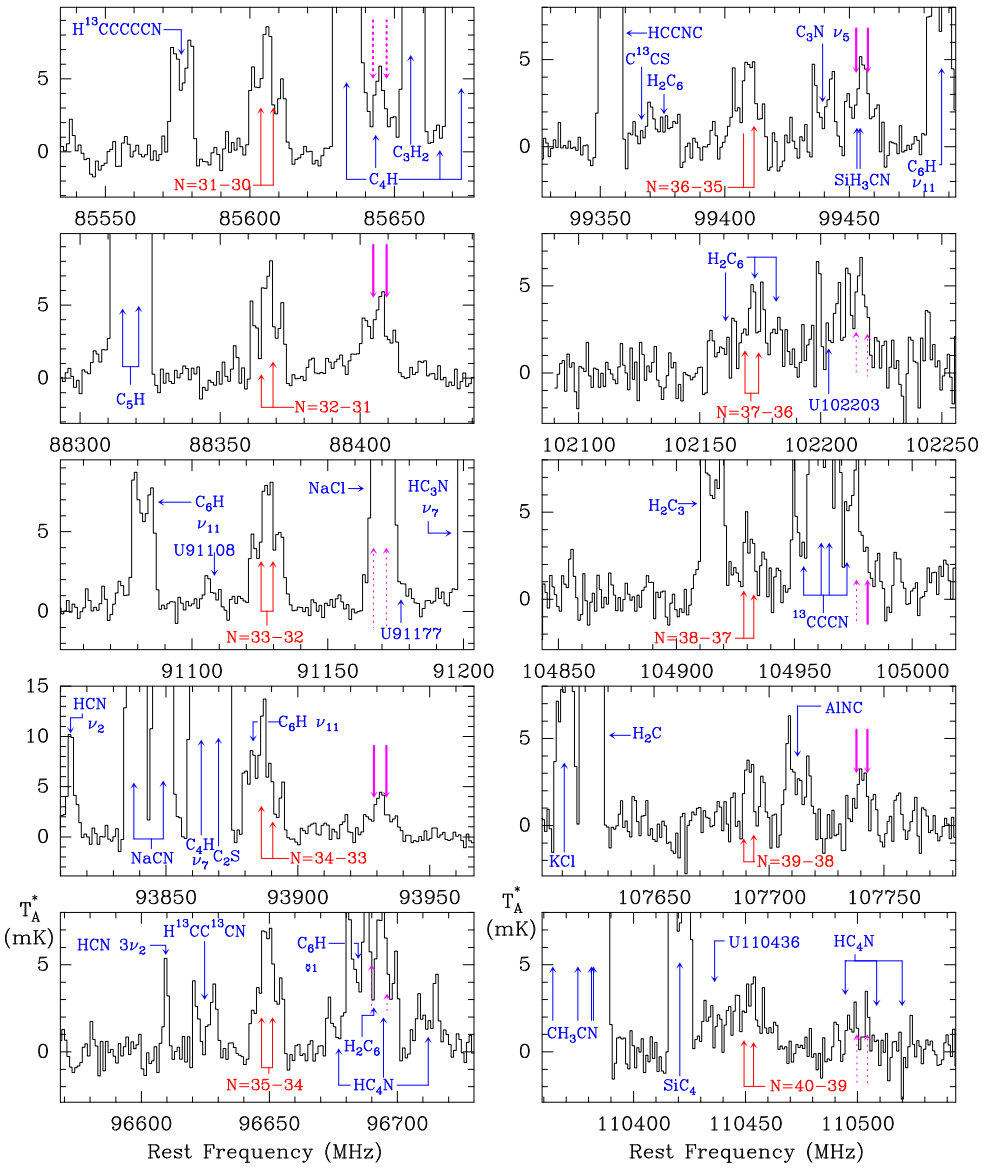

Fig. 2. Same as in Fig. 1, but for the doublets in the 3 mm domain observed with the IRAM 30 m radio telescope.

(36 ± 6 K), which is consistent with the line intensity distribution quoted above, and a column density of (2.2 ± 0.5) × 10^{13} cm^{-2}. The determination of column densities can be quite uncertain if infrared pumping (IR) plays a role in the excitation of the rotational levels (see Appendix D). These effects could be particularly important for molecules having low-frequency bending modes such as HC_3N, HC_5N, C_4H, MgC_3N, and MgC_4H (see Appendix D). Nevertheless, our two magnesium-bearing species have similar low-frequency bending modes (see Tables C.3 and C.4) and we could expect to have similar effects in the infrared pumping of their rotational levels. Therefore, the ratio of column densities MgC_4H/MgC_3N ~2.5 should not be greatly affected by IR pumping effects. On the other hand, the abundance ratio $MgC_4H/MgCCH$ ~10 may be overestimated if IR pumping is important for MgC_4H (see Appendices D and E). It is true that it seems counterintuitive to have a higher abundance for MgC_4H than for MgCCH, but in the chemical model discussed below everything depends on the branching ratios of the different fragmentation channels in the dissociative recombination of the $MgC_{2n}H_2^+$ complexes, which are difficult to anticipate (see below). Usually, within a given chemical family, larger molecules tend to be less abundant in IRC+10216. However, the anions C_nH^-, for which their synthesis also relies on the radiative association of C_nH radicals and electrons, show an increase in abundance with the number of carbon atoms.

In order to investigate the formation of the various magnesium cyanides and acetylides detected in IRC +10216 (MgNC, MgCN, HMgNC, MgC_3N, MgCCH, and MgC_4H) we carried out chemical model calculations based on the model of the outer envelope by Agúndez et al. (2017). As in previous models dealing with the formation of metal-bearing molecules in the outer shells of IRC +10216 (Millar 2008; Cabezas et al. 2013; Cernicharo et al. 2019), the synthesis relies on a two-step mechanism starting with the radiative association of Mg^+ with large cyanopolyynes and polyynes and the subsequent dissociative recombination of the corresponding $Mg^+/NC_{2n+1}H$ and $Mg^+/C_{2n}H_2$ complexes with electrons (Petrie 1996).

The rate coefficients for the radiative associations of Mg^+ with polyynes and cyanopolyynes were taken from the calculations by Dunbar & Petrie (2002). We consider that open-shell metal-containing species (MgNC, MgCN, MgC_3N, MgCCH, and MgC_4H) react with electrons and H atoms, while closed-shell molecules (HMgNC) do not. The branching ratios

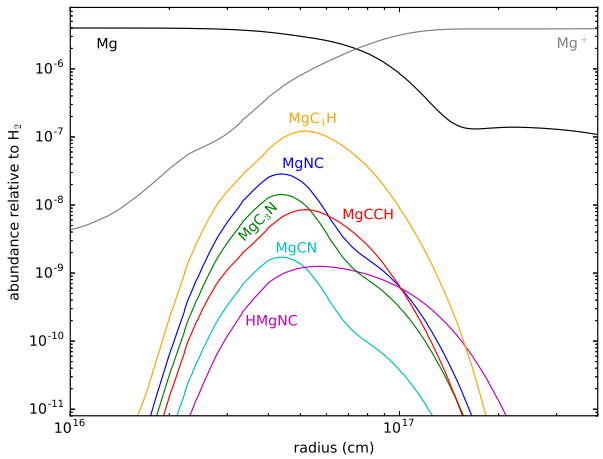

Fig. 3. Abundances calculated with the chemical model for the different Mg-bearing molecules detected in IRC +10216.

of the different fragmentation channels in the dissociative recombination of the $Mg^+/NC_{2n+1}H$ and $Mg^+/C_{2n}H_2$ ions are not known. We have therefore adjusted them to obtain column density ratios in agreement with those derived from observations. We find that in order to reproduce the relative column densities of the magnesium cyanides, the branching ratios of the channels yielding HMgNC, MgCN, and MgC_3N should respectively be 0.01, 0.05, and 0.7 of that yielding MgNC. In the case of the magnesium acetylides, the branching ratio of the channel producing MgCCH should be 0.1 of that yielding MgC_4H. It is curious that while MgNC is slightly more abundant than MgC_3N, in the case of magnesium acetylides the larger molecule MgC_4H is significantly more abundant than MgCCH. If the conclusion of $MgC_4H/MgCCH > 1$ is not in error due to IR pumping effects, this should be a consequence of the different behaviour in the fragmentation of $Mg^+/C_{2n}H_2$ complexes with respect to $Mg^+/NC_{2n+1}H$.

The absolute column densities of the Mg-bearing molecules are approximately reproduced (calculated column densities for MgC_3N and MgC_4H are 5.4×10^{12} and 3.6×10^{13} cm^{-2}, respectively) adopting an initial abundance of Mg relative to H of 1.5×10^{-6}, which is about 4% of the cosmic abundance of Mg. This value is higher than that used by Cabezas et al. (2013), mainly because in this model we include more metals (Mg, Na, Al, and Ca) and the new and abundant detected molecule MgC_3N must be accounted for. Unfortunately, Mauron & Huggins (2010) did not observe atomic Mg in the outer layers of IRC +10216, and therefore we do not have constraints on the abundance of atomic Mg. The results from the chemical model are shown in Fig. 3. In general, the two-step mechanism of Petrie (1996) can account for the formation of Mg cyanides and acetylides in IRC +10216. The main uncertainty is related to the branching ratios of the different fragmentation channels in the dissociative recombination of the cationic metal complexes, something that would be worth investigating in detail in the future.

Acknowledgements. The Spanish authors thank the Ministerio de Ciencia Innovación y Universidades for funding support from the CONSOLIDER-Ingenio program "ASTROMOL" CSD 2009-00038, AYA2012-32032, AYA2016-75066-C2-1-P. We also thank ERC for funding through grant ERC-2013-Syg-610256-NANOCOSMOS. MA thanks the Ministerio de Ciencia Innovación y Universidades for the Ramón y Cajal grant RyC-2014-16277. CB thanks the Ministerio de Ciencia Innovación y Universidades for the Juan de la Cierva grant FJCI-2016-27983. LVP acknowledges support from the Swedish Research Council and from ERC consolidator grant 614264.

References

Adler, T. B., Knizia, G., & Werner, H. J. 2007, J. Chem. Phys., 127, 221106
Agúndez, M., & Cernicharo, J. 2006, ApJ, 650, 374
Agúndez, M., Fonfría, J. P., Cernicharo, J., et al. 2008, A&A, 479, 493
Agúndez, M., Cernicharo, J., & Guélin, M. 2014, A&A, 570, A45
Agúndez, M., Cernicharo, J., Quintana-Lacaci, G., et al. 2015, ApJ, 814, 143
Agúndez, M., Cernicharo, J., Quintana-Lacaci, G., et al. 2017, A&A, 601, A4
Aoki, K. 2000, Chem. Phys. Lett., 323, 55
Bacalla, X., Salumbides, E. J., Linnartz, H. H., et al. 2016, J. Phys. Chem. A, 120, 6402
Bjorvatten, T. 1974, J. Mol. Struct., 20, 75
Brewster, M. A., Apponi, A. J., Xin, J., & Ziurys, L. M. 1999, Chem. Phys. Lett., 310, 411
Cabezas, C., Cernicharo, J., Alonso, J. L., et al. 2013, ApJ, 775, 133
Cabezas, C., Barrientos, C., Largo, A., et al. 2014, J. Chem. Phys., 141, 104305
Cabezas, C., Barrientos, C., Largo, A., et al. 2019, J. Chem. Phys., 151, 054312
Castor, J. I. 1970, MNRAS, 149, 111
Cernicharo, J. 1985, Internal IRAM report (Granada: IRAM)
Cernicharo, J. 2012, in ECLA 2011: Proc. of the Europ. Conf. on Laboratory Astrophysics, eds. C. Stehlé, C. Joblin, & L. d'Hendecourt, EAS Pub. Ser., 58, 251
Cernicharo, J., & Guélin, M. 1987, A&A, 183, L10
Cernicharo, J., Guélin, M., Kahane, C., et al. 1991, A&A, 246, 213
Cernicharo, J., Guélin, M., & Kahane, C. 2000, A&AS, 142, 181
Cernicharo, J., Guélin, M., & Pardo, J. R. 2004, ApJ, 615, L145
Cernicharo, J., Guélin, M., Agúndez, M., et al. 2007, A&A, 467, L37
Cernicharo, J., Guélin, M., Agúndez, M., et al. 2008, ApJ, 688, L83
Cernicharo, J., Teyssier, D., Quintana-Lacaci, G., et al. 2014, ApJ, 796, L21
Cernicharo, J., Marcelino, N., Agúndez, M., & Guélin, M. 2015, A&A, 575, A91
Cernicharo, J., Guélin, M., Agúndez, M., et al. 2018, A&A, 618, A4
Cernicharo, J., Velilla-Prieto, L., Agúndez, M., et al. 2019, A&A, 627, L4
Chasovskikh, E., Jochnowitz, E. B., & Maier, J. P. 2008, J. Phys. Chem. A, 112, 8686
Ding, H., Apetrei, C., Chacaga, L., & Maier, J. P. 2008, ApJ, 677, 348
Dunbar, R. C., & Petrie, S. 2002, ApJ, 564, 792
Forthomme, D., Linton, C., Tokaryk, D. W., et al. 2010, Chem. Phys. Lett., 488, 116
Frisch, M. J., Trucks, G. W., Schlegel, H. B., et al. 2016, Gaussian 16, Rev. A.03
Gou, X., Zhang, J., Li, J., et al. 2009, Chem. Phys., 360, 27
Guélin, M., Lucas, R., & Cernicharo, J. 1993, A&A, 280, L19
Guélin, M., Muller, S., Cernicharo, J., et al. 2000, A&A, 363, L9
Guélin, M., Muller, S., Cernicharo, J., et al. 2004, A&A, 426, L49
Hill, J. G., & Peterson, K. A. 2010, Phys. Chem. Chem. Phys., 12, 10460
Hill, J. G., Mazumder, S., & Peterson, K. A. 2010, J. Chem. Phys., 132, 054108
Jerosimić, S., Wester, R., & Gianturco, F. A. 2019, Phys. Chem. Chem. Phys., 21, 11405
Kawaguchi, K., Kagi, E., Hirano, T., et al. 1993, ApJ, 406, L39
Kawaguchi, K., Kasai, Y., Ishikawa, S., & Kaifu, N. 1995, Pub. Astron. Soc. Japan, 47, 853
Knizia, G., Adler, T. B., & Werner, H. J. 2009, J. Chem. Phys., 130, 054104
Mauron, N., & Huggins, P. J. 2010, A&A, 513, A31
McCarthy, M. C., Apponi, A. J., Gottlieb, C. A., et al. 2001, J. Chem. Phys., 115, 870
Millar, T. J. 2008, Ap&SS, 313, 223
Pardo, J. R., Cernicharo, J., & Serabyn, E. 2001, IEEE Trans. Antennas Propagation, 49, 12
Pardo, J. R., Cernicharo, J., Velilla-Prieto, L., et al. 2018, A&A, 615, L4
Petrie, S. 1996, MNRAS, 282, 807
Petrie, S. 1999, MNRAS, 302, 482
Petrie, S., Kagi, E., & Kawaguchi, K. 2003, MNRAS, 343, 209
Pulliam, R. L., Savage, C., Agúndez, M., et al. 2010, ApJ, 725, L181
Quintana-Lacaci, G., Agúndez, M., Cernicharo, J., et al. 2016, A&A, 592, A51
Sobolev, V. V. 1960, Moving Envelopes of Stars (Cambridge: Harvard University Press)
Sumiyoshi, Y., Katoh, K., & Endo, Y. 2005, Chem. Phys. Lett., 414, 82
Turner, B., Steimle, T. C., & Meerts, L. 1994, ApJ, 426, L97
Umeki, H., Nakajima, M., & Endo, Y. 2014, J. Chem. Phys., 141, 184303
Velilla, Prieto L., Cernicharo, J., Quintana-Lacaci, G., et al. 2015, ApJ, 805, L13
Werner, H. J., Knowles, P. J., Knizia, G., et al. 2018, MOLPRO, version 2018.1.
Zack, L. N., Halfen, D. T., & Ziurys, L. M. 2011, ApJ, 733, L36
Ziurys, L. M., Apponi, A. J., Guélin, M., & Cernicharo, J. 1995, ApJ, 445, L47
Ziurys, L. M., Savage, C., Highberger, J. L., et al. 2002, ApJ, 564, L45

Appendix A: Line frequencies

Table A.1. Observed rotational transitions of $S\,1$ (MgCCCN).

N_u [a]	J_u [a]	N_l [a]	J_l [a]	Obs.Freq. [b]	Unc. [c]	O-C [d]	Int. [e]
12	11.5	11	10.5	33138.673	0.150	0.075	0.169
12	12.5	11	11.5	33143.008	0.150	0.057	
13	12.5	12	11.5	35900.260	0.080	0.030	0.163
13	13.5	12	12.5	35904.683	0.080	0.100	
14	13.5	13	12.5	38661.866	0.150	0.027	0.245
14	14.5	13	13.5	38666.200	0.150	0.008	
15	14.5	14	13.5	41423.336	0.080	−0.086	0.257
15	15.5	14	14.5	41427.711	0.080	−0.064	
16	15.5	15	14.5	44185.057	0.150	0.079	0.259
16	16.5	15	15.5	44189.232	0.150	−0.099	
17	16.5	16	15.5	46946.648	0.150	0.143	0.275
17	17.5	16	16.5	46950.712	0.150	−0.146	
18	17.5	17	16.5	49708.020	0.150	0.020	0.339
18	18.5	17	17.5	49712.338	0.150	−0.015	
26	25.5	25	24.5	71798.763	0.150	0.131	0.329
26	26.5	25	25.5	71802.981	0.150	−0.003	
27	26.5	26	25.5	74559.941	0.300	0.175 [f]	0.340
27	27.5	26	26.5	74564.197	0.150	0.078	
28	27.5	27	26.5	77320.562	0.200	−0.290 [g]	
28	28.5	27	27.5	77324.925	0.200	−0.290 [g]	
29	28.5	28	27.5	[80081.886]	[0.032]	*n.i.* [h]	
29	29.5	28	28.5	80086.523	0.500	0.284 [i]	
30	29.5	29	28.5	82842.847	0.150	−0.020	0.255
30	30.5	29	29.5	82847.014	0.150	−0.207	
31	30.5	30	29.5	85603.749	0.150	−0.046	0.210
31	31.5	30	30.5	85608.518	0.150	0.370	
32	31.5	31	30.5	88364.669	0.150	0.004	0.242
32	32.5	31	31.5	88369.040	0.150	0.022	
33	32.5	32	31.5	91125.390	0.150	−0.087	0.279
33	33.5	32	32.5	91129.844	0.150	0.014	
34	33.5	33	32.5	[93886.229]	[0.042]	*n.i.* [j]	0.279
34	34.5	33	33.5	93890.277	0.200	−0.305	
35	34.5	34	33.5	96646.999	0.150	0.080	0.227
35	35.5	34	34.5	96651.440	0.150	0.168	
36	35.5	35	34.5	99407.472	0.200	−0.073	0.166
36	36.5	35	35.5	99411.815	0.200	−0.083	
37	36.5	36	35.5	102168.400	0.500	0.295	
37	37.5	36	36.5	[102172.458]	[0.055]	*n.i.* [k]	
38	37.5	37	36.5	104928.720	0.500	0.122 [l]	0.133
38	38.5	37	37.5	104932.450	0.500	−0.501 [l]	
39	38.5	38	37.5	107688.500	0.500	−0.522 [l]	0.103
39	39.5	38	38.5	107693.827	0.500	0.452 [l]	
40	39.5	39	38.5	110449.410	0.500	0.035 [l]	0.131
40	40.5	39	39.5	110453.977	0.500	0.249 [l]	

Notes. [a]Quantum numbers N and J of the rotational transition. The subindex u means upper level and l lower level. [b]Observed frequency in MHz. Square brackets indicate a calculated frequency. [c]Uncertainty assigned to the measured frequency in MHz. Square brackets indicate a calculated uncertainty from the fit. [d]Observed frequency minus calculated frequency from the fit in MHz. If *n.i.* the line is not included in the fit. [e]Main beam temperature integrated over the LSR velocity, in K km s^{-1}. The uncertainties are below 15%. [f]Line marginally blended with HC_5N. [g]Line blended with narrow U feature. [h]Line fully blended with HC_7N. [i]Line partially blended with HC_7N. [j]Line blended with C_6H in ν_{11} mode. [k]Line fully blended with H_2C_6. [l]Weak feature.

Line frequencies were determined by fitting the observed lines with a specific line profile typical of expanding envelopes. The sharp edges of the lines permit us to fit their central frequencies, even when signals are weak, with an accuracy well below 0.5 MHz (Cernicharo et al. 2018). Only when lines are heavily blended is it not possible to accurately derive their frequencies, or even to fit them. Two of the $S\,1$ doublets are heavily blended (N = 29–28 and 37–36). Some doublets (N = 17–16, 27–26, 28–27, and 34–33) show some blending, but the frequencies can still be derived by fixing the linewidths to 29 km s^{-1} (Cernicharo et al. 2000, 2018). The signal-to-noise ratio for the doublets N = 39–38 and 40–39 is low, and therefore we assigned a large uncertainty to their frequencies. We note that due to the increase in linewidth (in MHz) with frequency, the pair of lines of each doublet start to overlap for $N_{up} > 16$. Table A.1 gives the observed and fitted line frequencies for $S\,1$. The series of doublets $S\,2$ are only detected in the 3 mm data. They also show significant blending with other features, as indicated in Figs. 1 and 2. Observed and fitted line frequencies for these doublets are given in Table A.2. The intensity of the observed lines is also provided in the tables.

Table A.2. Observed rotational transitions of $S\,2$ (MgC_4H).

N_u [a]	J_u [a]	N_l [a]	J_l [a]	Obs.Freq. [b]	Unc. [c]	O-C [d]	Int. [e]
26	25.5	25	24.5	71830.149	1.000	−0.943 [f]	0.155
26	26.5	25	25.5	71835.629	0.500	−0.147	
27	26.5	26	25.5	74593.987	0.300	0.492	0.147
27	27.5	26	26.5	74597.613	0.300	−0.566	
28	27.5	27	26.5	77355.466	0.300	−0.384	
28	28.5	27	27.5	77361.172	0.300	0.638	
29	28.5	28	27.5	80118.288	0.300	0.133	0.154
29	29.5	28	28.5	80122.274	0.500	*n.i.* [g]	
30	29.5	29	28.5	[82880.409]	[0.081]	*n.i.* [h]	
30	30.5	29	29.5	[82885.093]	[0.082]	*n.i.* [h]	
31	30.5	30	29.5	[85642.610]	[0.078]	*n.i.* [i]	
31	31.5	30	30.5	[85647.294]	[0.076]	*n.i.* [i]	
32	31.5	31	30.5	88404.483	0.200	−0.273	0.164
32	32.5	31	31.5	88409.447	0.200	0.007	
33	32.5	32	31.5	[91166.845]	[0.078]	*n.i.* [j]	
33	33.5	32	32.5	[91171.529]	[0.070]	*n.i.* [j]	
34	33.5	33	33.5	93929.043	0.200	0.166	0.136
34	34.5	33	33.5	93933.779	0.200	0.219	
35	34.5	34	33.5	[96690.848]	[0.092]	*n.i.* [k]	
35	35.5	34	34.5	[96695.531]	[0.079]	*n.i.* [k]	
36	35.5	35	34.5	99452.794	0.500	0.037 [l]	0.151
36	36.5	35	35.5	99457.396	0.200	−0.044	
37	36.5	36	35.5	[102214.602]	[0.121]	*n.i.* [g]	
37	37.5	36	36.5	[102219.286]	[0.105]	*n.i.* [g]	
38	37.5	37	36.5	[104976.382]	[0.140]	*n.i.* [m]	0.105
38	38.5	37	37.5	104981.775	1.000	0.709 [m]	
39	38.5	38	37.5	107738.266	0.500	0.171	0.082
39	39.5	38	38.5	107741.955	0.500	−0.824	
40	39.5	39	38.5	[110499.739]	[0.186]	*n.i.* [h]	0.074
40	40.5	39	39.5	[110504.422]	[0.169]	*n.i.* [h]	

Notes. [a]Quantum numbers N and J of the rotational transition. The subindex u means upper level and l lower level. [b]Same as in Table A.1. [c]Same as in Table A.1. [d]Observed frequency minus calculated frequency from the fit in MHz. If *n.i.* the line is not included in the fit. [e]Main beam temperature integrated over the LSR velocity, in K km s^{-1}. The uncertainties are below 30%. [f]Line contaminated with KCN. [g]Line contaminated with a U-line. [h]Line contaminated with HC_4N. [i]Line contaminated with C_4H. [j]Line contaminated with NaCl. [k]Line contaminated with several features. [l]Line contaminated with SiH_3CN. [m]Line contaminated with $^{13}CCCN$.

Appendix B: Possible carriers of the *S*1 and *S*2 series

The very close rotational constants of $S\,1$ and $S\,2$ could suggest that they belong to a common molecular carrier. However, the dependence of the line intensity with N is very different. In the case of $S\,2$, low N lines are weak and marginally detected in the Q band, while high N lines are clearly detected in the 3 mm domain; instead, for $S\,1$ the lines are well detected in the Q band and start to vanish at the high end of the 3 mm band. Clearly the two series of doublets arise from two molecular species with different permanent dipole moments. Moreover, the possibility that $S\,2$ is a bending state of $S\,1$ seems very unlikely for the same reasons and because this state will have a $^2\Pi$ vibronic character. In addition, if $S\,2$ were a bending state of $S\,1$ we could expect another series of doublets as the bending introduces an l-doubling as occurs in linear $^1\Sigma$ molecules. The expected value of q, the l-doubling parameter, is a few tens of MHz. Hence, we searched in our data for other series with the same splitting of 4.7 MHz. No obvious candidates were found for a range of 2000 MHz around each observed doublet of $S\,2$.

The difference in line intensities also precludes the possibility that $S\,1$ and $S\,2$ could correspond to the four components of the rotational transitions $N \rightarrow N-1$ of a $^4\Sigma$ electronic state. For such a carrier, the intensities of the four components are proportional to $J(\boldsymbol{J = N + S})$, hence very similar for the values of N involved in our data. Moreover, this possible carrier needs to have a rather low spin-spin interaction constant in view of the very close frequencies of the four components for each rotational quantum number N.

The rotational constants of $S\,1$ and $S\,2$ are very close to those of well-known molecular species in this source: HC_5N, C_6H, C_5N^-, and C_5N. However, the distortion constants are a factor of 1.4–2 higher for our doublets than for these species. C_6H has several bending modes. The $^2\Sigma^-$ state of the mode ν_{11} of C_6H, which shows a series of doublets with integer harmonic relations, has been characterized in this source (Cernicharo et al. 2008). The corresponding $^2\Sigma^+$ state could be higher in energy and with frequencies very close to those of the $^2\Sigma^-$ state (Cernicharo et al. 2008). The ν_{10} mode also has a relatively low energy, ~200 cm^{-1} (Bacalla et al. 2016). It will also be split into a $^2\Sigma^-$ and a $^2\Sigma^+$ state, in addition to a $^2\Delta$ state with half integer quantum numbers. However, as for any bending mode, we expect to have a rotational constant larger than for the ground state of the molecule. The $S\,1$ and $S\,2$ doublets have rotational constants lower than that of C_6H in its ground state. Hence, these doublets cannot be assigned to vibrationally excited C_6H in its ν_{10} mode. Moreover, $S\,1$ and $S\,2$ cannot be assigned to the ν_{11} modes of ^{13}C isotopically substituted C_6H as the $^{12}C/^{13}C$ abundance ratio in this source is ~42 (Cernicharo et al. 1991), and the observed $S\,1$ and $S\,2$ intensities are similar to those of the lines of the ^{13}C isotopologues of C_6H in their ground vibrational state. In addition, six series of doublets, with identical intensity and line separation, could be expected from the ν_{11} vibrational state of the ^{13}C isotopologues of C_6H. The same applies to C_5N, which has a rotational constant larger than C_6H.

The anion HC_5N has been calculated to have a ^2A ground electronic state with $(B + C)/2$ ~1377 MHz (Jerosimić et al. 2019). The calculation method is very similar to the one used in this work, RHF-CCSD(T)-F12/cc-pVTZ-F12. HC_5N^- would only be compatible with the $S\,1$ or $S\,2$ doublets if we were observing the $K_a = 0$ transitions of HC_5N^-. In this case the effective distortion constant for this asymmetric species would be larger than those obtained for the $S\,1$ and $S\,2$ doublets. We calculated the theoretical value for D_N because it was not reported in the Jerosimić et al. (2019) work at the CCSD(T)/cc-pVTZ level of theory, and we found $D_N = 0.28$ kHz, almost 4–5 times higher than those of $S\,1$ and $S\,2$. This value is totally incompatible with our experimental values of D for $S\,1$ and $S\,2$. Hence, HC_5N^- cannot be considered as a candidate. In addition, we calculated the spin-rotation constants of HC_5N^-, which are 1203.4, −0.2, and −2.5 MHz for ϵ_{aa}, ϵ_{bb}, and ϵ_{cc}, respectively. They are also different from our experimental value of γ. ClCCCN has a rotational constant of 1382 MHz (Bjorvatten 1974), which is very close to those of $S\,1$ and $S\,2$, although this species has a $^1\Sigma$ ground electronic state. ClC_4 has a $^2\Sigma$ ground electronic state. However, its rotational constant is 1455.6 MHz (Sumiyoshi et al. 2005). SiC_4H (McCarthy et al. 2001) and SiC_3N (Umeki et al. 2014) have a rotational constant of 1415.7 and 1414.7 MHz, respectively, and they have a $^2\Pi$ electronic state.

Petrie (1999) suggested that the species $M-C_3N$ could be abundant in IRC +10216. Two of these species, AlC_3N and NaC_3N, have been observed in the laboratory by Cabezas et al. (2019). They have $^1\Sigma$ ground electronic states and rotational constants close to those of $S\,1$ and $S\,2$ (1340.8 and 1321.1 MHz, respectively). They have been searched for in IRC +10216 without success. Petrie et al. (2003) performed quantum chemical calculations and provided estimations for the rotational constants of MgC_3N and MgC_4H. Both molecules have a $^2\Sigma$ ground electronic state and the calculated rotational constants are very close to those of $S\,1$ and $S\,2$.

Appendix C: Quantum chemical calculations of MgC_3N and MgC_4H

MgC_3N and MgC_4H have already been investigated by quantum chemical calculations at diverse levels of theory, and some theoretical works are available in the literature (Petrie et al. 2003; Ding et al. 2008; Gou et al. 2009; Forthomme et al. 2010; Cabezas et al. 2019). However, in an attempt to obtain the most precise geometries and spectroscopic molecular parameters for the species MgC_3N and MgC_4H, we performed high-level ab initio calculations using very accurate methods and basis sets.

Further evidence in support of the assignment of MgC_3N to $S\,1$ and MgC_4H to $S\,2$ is related to the constants D and γ. The predicted values, with the geometries optimized either at the CCSD(T)-F12/cc-pCVTZ-F12 or CCSD(T)/aug-cc-pVTZ level, are in very good agreement with those derived from the observations. In addition, a similar comparison of the MgC_3N/MgC_4H constant ratios can be made with the data of Table C.1 and the agreement is almost perfect for both D and γ.

All structure optimization calculations reported in this work were performed using both the spin-restricted open-shell coupled cluster with single, double, and perturbative triple excitations (CCSD(T)) with and without an explicitly correlated (F12) approximation (Adler et al. 2007; Knizia et al. 2009). The Dunning's augmented correlation consistent polarized valence triple-ζ (aug-cc-pVTZ) basis set, where only valence electrons are correlated, was used with the CCSD(T) method. On the other hand, with the calculations at the CCSD(T)-F12 level, the Dunning's correlation consistent basis sets with polarized core-valence correlation triple-ζ for explicitly correlated calculations (cc-pCVTZ-F12; Hill et al. 2010; Hill & Peterson 2010) was used. In this latter case, all electrons (valence and core) were correlated. Using both levels of theory, the equilibrium molecular geometries, rotational constants, and dipole moments μ were calculated for MgC_3N and MgC_4H in their ground

Table C.1. Comparison of experimental and theoretical values for the spectroscopic parameters of MgCCCN and MgCCCCH.

MgCCCN	Exp. [a]	CCSD(T)-F12 [b]	CCSD(T) [c]
B /MHz	1380.888(1)	1376.4990[0.3]	1357.6663[1.7]
D /kHz	0.0760(5)	0.0644[15.3] [d]	0.0649[14.6]
γ/MHz	4.35(4)	4.09[5.9] [e]	3.93[9.7] [f]
μ /D		6.38	6.39
MgCCCCH	Exp. [a]	CCSD(T)-F12[b]	CCSD(T) [c]
B /MHz	1381.512(4)	1377.3833[0.3]	1358.4109[1.7]
D /kHz	0.074(2)	0.0605[18.2] [d]	0.0614[17.0]
γ/MHz	4.7(1)	4.43[5.7] [e]	4.24[9.8] [f]
μ /D		2.12	2.16
Ratio [g]	Exp. [a]	CCSD(T)-F12 [b]	CCSD(T) [c]
B	0.9996	0.9994	0.9995
D	1.0270	1.0645 [d]	1.0576 [d]
γ	0.9255	0.9238 [e]	0.9266 [e]

Notes. Numbers in parentheses are 1σ uncertainties in units of the last digits. Numbers in square brackets are the percentage of relative error calculated as (experimental−theoretical)/experimental. [a]This work. [b]Calculated at the CCSD(T)-F12/cc-pCVTZ-F12 level of theory. [c]Quantum chemical calculation results at the CCSD(T)/aug-cc-pVTZ level of theory. [d]Calculated at the CCSD(T)/cc-pVTZ level of theory. [e]Calculated at the MP2/cc-pVTZ level of theory. [f]Calculated at the MP2/aug-cc-pVTZ level of theory. [g]Ratio MgCCCN/MgCCCCH of the spectroscopic constant.

Table C.2. Comparison of experimental and theoretical values for the spectroscopic parameters of MgCCH.

MgCCH	Exp. [a]	CCSD(T)-F12 [b]	CCSD(T) [c]
B /MHz	4965.335(4)	4947.373[0.4]	4864.358[2.0]
D /kHz	2.232(2)	1.886[15.5] [d]	1.933[13.4]
γ/MHz	16.49(4)	15.72[4.7] [e]	15.02[8.9][f]

Notes. Numbers in parentheses are 1σ uncertainties in units of the last digits. Numbers in square brackets are the percentage of relative error calculated as (experimental−theoretical)/experimental. [a]Brewster et al. (1999). [b]Calculated at the CCSD(T)-F12/cc-pCVTZ-F12 level of theory. [c]Calculated at the CCSD(T)/aug-cc-pVTZ level of theory. [d]Calculated at the CCSD(T)/cc-pVTZ level of theory. [e]Calculated at the MP2/cc-pVTZ level of theory. [f]Calculated at the MP2/aug-cc-pVTZ level of theory.

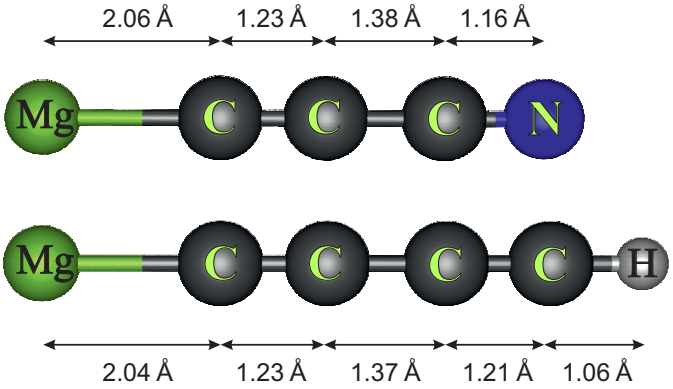

Fig. C.1. MgCCCN (*top*) and MgCCCCH (*bottom*) optimized structures at the CCSD(T)-F12/cc-pCVTZ-F12 level of theory.

electronic states using the Molpro 2018.1 ab initio program package (Werner et al. 2018).

An important molecular parameter needed to precisely simulate the rotational spectra of MgC_3N and MgC_4H at the observed frequency regions is the centrifugal distortion constant (D). This constant was obtained by subsequent harmonic vibrational calculations at the CCSD(T)/cc-pVTZ and CCSD(T)/aug-cc-pVTZ levels of theory. Since MgC_3N and MgC_4H are open-shell species, the spin-rotation constant γ is another parameter to take into account to adequately estimate the transition rotational frequencies. It was calculated at the MP2/cc-pVTZ and MP2/aug-cc-pVTZ levels of theory using the optimized structures at the CCSD(T)-F12/cc-pCVTZ-F12 and CCSD(T)/aug-cc-pVTZ levels of theory, respectively. We used different calculations methods for D and γ because they cannot be calculated with explicitly correlated methods, and thus the Gaussian 16 program package was used (Frisch et al. 2016).

Although MgC_3N and MgC_4H present different structural isomers, i.e. linear, cyclic, or T-shaped (Petrie et al. 2003; Cabezas et al. 2019), we only considered the lowest energy isomers with $^2\Sigma^+$ linear structures: MgCCCN and MgCCCCH. The geometry optimizations were done at both the CCSD(T)/aug-cc-pVTZ and CCSD(T)-F12/cc-pCVTZ-F12 methods, because the data obtained with the latter method was the most accurate. It has been demonstrated (Adler et al. 2007; Knizia et al. 2009) that the F12 correction strongly improves the basis set convergence for a wide variety of applications, including reaction energies of both open- and closed-shell reactions, atomization energies, electron affinities, equilibrium geometries, or harmonic vibrational frequencies. In addition, correlation consistent basis sets such as cc-pCVTZ-F12 have been optimized for accurately describing core-core and core-valence correlation effects with explicitly correlated F12 methods.

The reliability of the two methods of calculation was tested in the case of MgCCH. The CCSD(T)/aug-cc-pVTZ and CCSD(T)-F12/cc-pCVTZ-F12 predicted rotational constants for MgCCH are 4864.36 and 4947.37 MHz, respectively, while the experimental value for MgCCH is 4965.3346 ± 0.0038 MHz (Brewster et al. 1999). The relative percentage deviation in the calculation, $(((B_{exp} - B_{th})/B_{exp}) \times 100)$, is 2.03% for CCSD(T)/aug-cc-pVTZ, but only 0.36% when CCSD(T)-F12/cc-pCVTZ-F12 is used. Therefore, it seems that the latter level of calculation is reliable for predictive purposes in magnesium-bearing compounds.

The constants D and γ were calculated for MgCCH and the results, shown in Table C.2, point to discrepancies that are substantially larger than for the rotational constant B. However, the values of D and γ calculated at the CCSD(T)/cc-pVTZ and MP2/cc-pVTZ levels are accurate enough, considering that the precise estimation of these values by ab initio calculations is complicated.

The results of our calculations for MgCCCN and MgCCCH are summarized in Table C.1 and the optimized geometries are shown in Fig. C.1. Tables C.3–C.5 show harmonic vibrational frequencies and infrared band intensities of MgCCCN, MgCCCCH, and MgCCH, respectively, calculated at the CCSD(T)/cc-pVTZ level of theory. As in the case of MgCCH, the errors between the experimental and calculated rotational constants at the CCSD(T)-F12/cc-pCVTZ-F12 level of theory are very small, 0.3% in both cases when MgCCCN and MgCCCH are assigned to $S1$ and $S2$, respectively. In the same way, the errors are larger when the CCSD(T)/aug-cc-pVTZ level is used, 1.7% for both MgCCCN and MgCCCCH, while for MgCCH it is 2.0%. This indicates that, independently of the level of the calculation, the assignments of MgCCCN to $S1$ and

Table C.3. Harmonic vibrational frequencies of MgCCCN calculated at the CCSD(T)/cc-pVTZ level.

Mode	Symmetry	Frequency (cm^{-1})	IR intensity [a] (km $mole^{-1}$)
1	π	76	0.16
2	π	257	6.43
3	σ	391	82.35
4	π	508	3.16
5	σ	933	75.71
6	σ	2083	15.86
7	σ	2299	3.54

Notes. [a]Intensities calculated at the MP2/aug-cc-pVTZ level of theory.

Table C.4. Harmonic vibrational frequencies of MgCCCCH calculated at the CCSD(T)/cc-pVTZ level.

Mode	Symmetry	Frequency (cm^{-1})	IR intensity [a] (km $mole^{-1}$)
1	π	71	6.94
2	π	253	0.10
3	σ	403	85.13
4	π	502	0.56
5	π	607	40.38
6	σ	949	62.00
7	σ	2033	53.86
8	σ	2213	2.72
9	σ	3460	95.99

Notes. [a]Intensities calculated at the MP2/aug-cc-pVTZ level of theory.

Table C.5. Harmonic vibrational frequencies of MgCCH calculated at the CCSD(T)/cc-pVTZ level.

Mode	Symmetry	Frequency (cm^{-1})	IR intensity [a] (km $mole^{-1}$)
1	π	156	11.82
2	σ	492	98.86
3	π	659	38.83
4	σ	2055	20.69
5	σ	3428	24.96

Notes. [a]Intensities calculated at the MP2/aug-cc-pVTZ level of theory.

MgCCCCH to $S2$ provides discrepancies of the same order, which supports the identification of these species. The same conclusion can be reached if we compare the ratios between the experimental rotational constants of MgCCCN ($S1$) and MgCCCCH ($S2$), $B_{exp}(MgC_3N)/B_{exp}(MgC_4H)$, with those obtained from the theoretical calculations, $B_{th}(MgC_3N)/B_{th}(MgC_4H)$. The ratio for the experimental rotational constants is 0.9996, while those for the CCSD(T)-F12/cc-pCVTZ-F12 and CCSD(T)/aug-cc-pVTZ levels, respectively, are 0.9994 and 0.9995, in excellent agreement with the experimental value.

Previous quantum chemical calculations for MgCCCN have been reported by Petrie et al. (2003) and Cabezas et al. (2019). In their work, Petrie et al. (2003) used the B3LYP, MP3, CCSD, and CCSD(T) methods in conjunction with some basis sets. The corrected value for the rotational constant of MgCCCN using CCSD(T)/cc-pVDZ is 1383.3 MHz, which is not far from the experimental value. Cabezas et al. (2019) calculated the rotational constant, with the estimated vibration-rotation interaction constants by second-order perturbation theory at the MP2/aug-cc-pVTZ level, and found an overestimated value of 1391.3 MHz, 0.75% higher than the experimental value.

Ding et al. (2008) and Gou et al. (2009) reported theoretical values for the rotational constant of MgCCCCH using B3LYP, RCCSD(T) and CASSCF methods. The values found by Ding et al. (2008) are 1382.5 MHz when using the B3LYP/aug-cc-pVTZ and 1351.4 MHz at the RCCSD(T)/aug-cc-pVTZ level of theory. The latter value is a bit lower than that reported in this work using the same level of theory, 1358.41 MHz. On the other hand, Gou et al. (2009) used more modest levels of theory and obtained B values of 1373.3 and 1360.8 MHz at the B3LYP/6-31G* and CASSCF/6-31G* levels.

Appendix D: The role of infrared pumping of polyatomic molecules

Infrared pumping of polyatomic molecules could strongly affect the population of the rotational levels of the ground vibrational state of the considered species. The pumping is produced by absorption of photons from a level J_{low} to a level of any of the ro-vibrational modes with total quantum number $J_{up} = J_{low} \pm 1$ ($\Delta J = 0$ transitions are also allowed if bending is considered), followed by fast decay to levels of the ground state with $J = J_{up} \pm 1$. These up and down radiative cascades can populate levels of high J that will normally be weakly pumped by collisions. Agúndez & Cernicharo (2006) showed that IR pumping in molecules like water can produce errors as large as a factor of ten in the determination of the column density. Similar effects apply to triatomic species such as CCH and HNC (Cernicharo et al. 2014).

The role of infrared pumping of the simple polyatomic molecule HNC has been analysed by Cernicharo et al. (2014). Each mode affects the pumping of the ground state in a different way as it depends on the vibrational intensity, the size of the IR emitting region, and the temperature of the dust. Infrared pumping through stretching modes (frequencies above 1000 cm^{-1}) is produced by photons arising from a warm and very small region (e.g. the dust formation zone for IRC+10216, which has a diameter <1″). However, the pumping through the bending states depends strongly on the frequency of the vibrational mode. The size of the emitting region for frequencies below 100 cm^{-1} can be much larger than those producing infrared pumping through the stretching modes.

In addition to the fundamental modes we have to consider all the combination modes involving two bendings, and one bending plus one stretching that are strongly radiatively connected to the ground. The number of infrared cascades increases considerably with the number of atoms. Agúndez et al. (2017) have performed some simple models for C_nH radicals and cyanopolyynes species ($HC_{2n+1}N$) showing that infrared pumping can modify the spatial distribution of each species and has a important effect on the observed intensities. MgC_3N has seven vibrational modes (see Table C.3), MgC_4H has nine (see Table C.4), while MgCCH has only only five (see Table C.5). Hence, while MgC_3N and MgC_4H could have similar infrared pumping effects, they could be very different to those of MgCCH. A detailed modelling is really complex and is beyond the scope of the present work. The derived column densities, and the MgC_4H/MgCCH abundance ratio, should be considered with caution.

Appendix E: Confirmation of MgCCH in space

MgCCH was tentatively detected by Agúndez et al. (2014) on the basis of the two doublets N = 9–8 and 10–9. Since these observations, additional data of IRC +10216 have been collected at 3 and 2 mm with the IRAM 30 m telescope (Cernicharo et al. 2018, 2019). The lines presented by Agúndez et al. (2014) at 3 mm are very weak (T_A^* ~2 mK) and the detection of additional doublets was only possible when the sensitivity of the data reached a level below 1 mK.

Figure E.1 shows the data for all doublets of MgCCH up to N = 17–16. The signal-to-noise ratio of the 3 mm data has improved and the two doublets N = 9–8 and 10–9 now appear at a high confidence level. Additional doublets without blending from other features are N = 15–14 and 16–15. For the N = 11–10 doublet, the J = N − 1/2 component is fully blended with a component of N = 1–0 transition of ^{13}CN. However, the J = N + 1/2 component is clearly detected. For the N = 13–12 doublet, although the bulk of the emission is blended with NaCN, the left side of J = N − 1/2 component is visible and the same happens for the right side of the J = N + 1/2 component. In the case of the N = 14–13 doublet only the J = N + 1/2 component appears clearly. Although the other component is marginally present, the sensitivity of the data and probable baseline problems at these noise levels prevent its confident detection. Finally, the N = 17–16 has a poor signal-to-noise ratio and the J = N − 1/2 component is partially blended with H_2S. However, the J = N + 1/2 component is detected with an intensity similar to that of the other doublets.

Hence, on the basis of four doublets and five additional features agreeing with the J = N − 1/2 or J = N + 1/2 components of other doublets, we conclude that MgCCH can be considered as detected in IRC +10216. We derive a column density for MgCCH identical to that derived by Agúndez et al. (2014), i.e. N(MgCCH) ~2×10^{12} cm^{-2}.

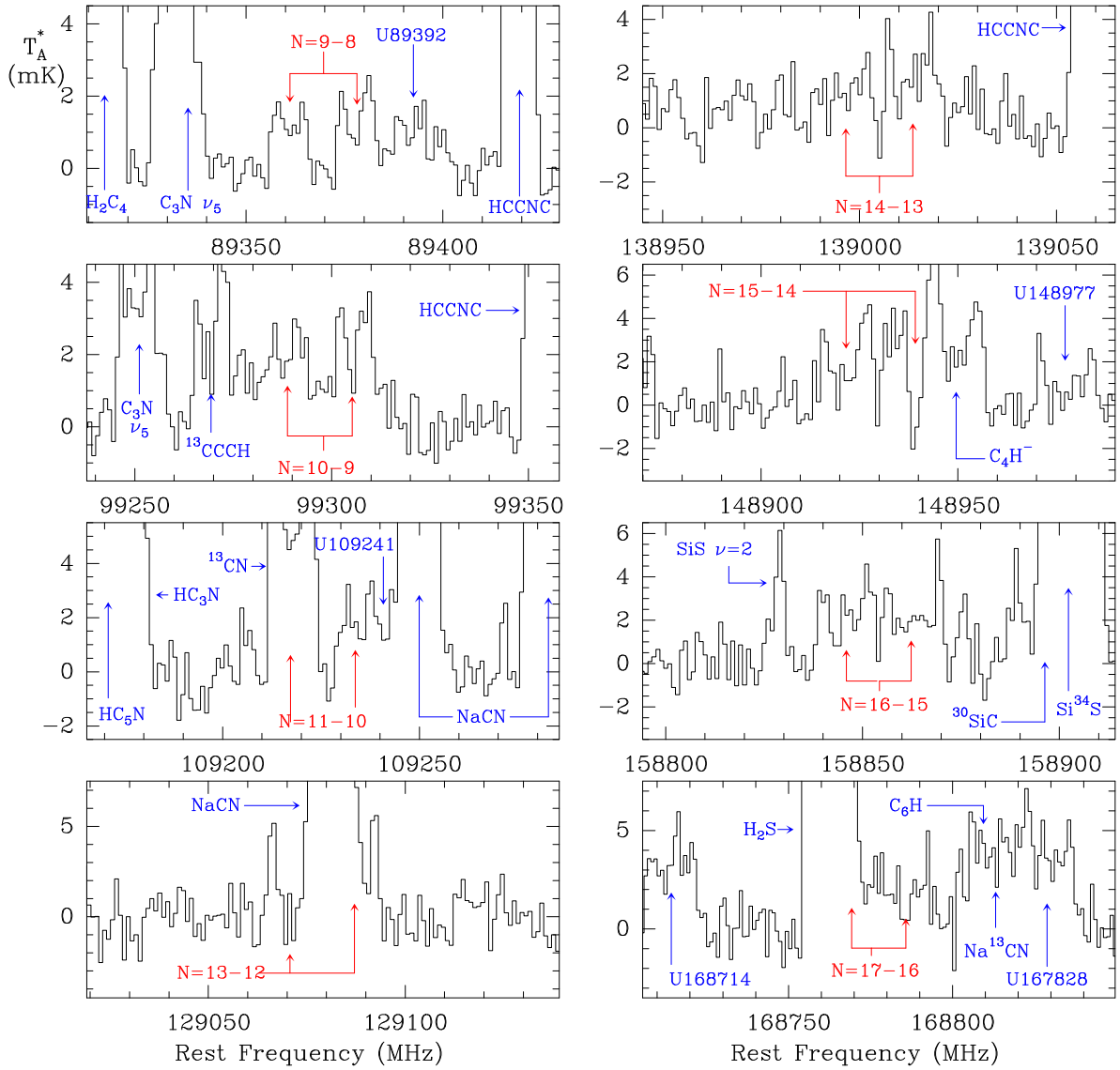

Fig. E.1. Observed doublets of MgCCH towards IRC+10216 (black histogram). The vertical scale is the antenna temperature in mK, and the horizontal scale is the frequency in MHz. Labels for the lines of MgCCH are plotted in red in each panel. Unidentified (U) lines are indicated in blue.